International Journal of Geo-Information

MDPI

Article

Geometric Characterization of the Mateur Plain in Northern Tunisia Using Vertical Electrical Sounding and Remote Sensing Techniques

Wissal Issaoui [1,2,3,*], Imen Hamdi Nasr [1,2], Dimitrios D. Alexakis [4], Wafa Bejaoui [1], Ismael M. Ibraheem [5], Ahmed Ezzine [3], Dhouha Ben Othman [3] and Mohamed Hédi Inoubli [2]

[1] Department of Earth Sciences, Faculty of Sciences of Bizerte 7021, University of Carthage Tunisia, Carthage 1054, Tunisia; imenhamdi79@yahoo.fr (I.H.N.); wafabejaouiwafa@gmail.com (W.B.)
[2] URGAMM-Faculty of Sciences of Tunis, University of Tunis El Manar 2092, Tunis 1938 , Tunisia; mh.inoubli@gmail.com
[3] National Center of Mapping and Remote Sensing, El Aouina 1080, Tunis 1938, Tunisia; ezzine.ah@gmail.com (A.E.); douhabenothman@hotmail.fr (D.B.O.)
[4] Institute for Mediterranean Studies, Foundation for Research and Technology Hellas, 70013 Iraklio, Greece; dalexakis@ims.forth.gr
[5] Institute of Geophysics and Meteorology, University of Cologne, 50923 Cologne, Germany; ismael.ibraheem@geo.uni-koeln.de
* Correspondence: wilala27972172@gmail.com

Abstract: The Mateur aquifer system in Northern Tunisia was examined using data from 19 water boreholes, 69 vertical electrical sounding (VES) stations, and a Sentinel-2 satellite image. Available boreholes and their corresponding logs were compared to define precisely the multi-layer aquifer system, including the Quaternary and Campanian aquifers of the Mateur plain. Quantitative interpretation and qualitative evaluation of VES data were conducted to define the geometry of these reservoirs. These interpretations were enhanced by remote sensing imagery processing, which enabled the identification of the Mateur plain's superficial lineaments. Based on well log information, the lithological columns show that the Quaternary series in the Ras El Ain region contains a layer of clayey, pebbly, and gravelly limestone. Additionally, in the Oued El Tine area, a clayey lithological unit has been identified as a multi-layer aquifer. The study area, exhibiting apparent resistivity values ranging between 20 and 170 Ohm·m, appears to be rich in groundwater resources. The correlation between the lithological columns and the interpreted VES data, presented as geoelectrical cross-sections, revealed variations in depth (8–106 m), thickness (10 to 55 m), and resistivity (20–98 Ohm·m) of a coarse unit corresponding to the Mateur aquifer. Twenty-three superficial lineaments were extracted from the Sentinel-2 image. Their common superposition indicated that both of them are in a good coincidence; these could be the result of normal faults, creating an aquifer system divided into raised and sunken blocks.

Keywords: Tunisia; Mateur plain; groundwater aquifer; vertical electrical sounding (VES); remote sensing; satellite image

Citation: Issaoui, W.; Nasr, I.H.; D. Alexakis, D.; Bejaoui, W.; Ibraheem, I.M.; Ezzine, A.; Ben Othman, D.; Inoubli, M.H. Geometric Characterization of the Mateur Plain in Northern Tunisia Using Vertical Electrical Sounding and Remote Sensing Techniques. *ISPRS Int. J. Geo-Inf.* **2024**, *13*, 333. https://doi.org/10.3390/ijgi13090333

Academic Editors: Wolfgang Kainz and Godwin Yeboah

Received: 17 July 2024
Revised: 6 September 2024
Accepted: 11 September 2024
Published: 18 September 2024

1. Introduction

Limited knowledge of an aquifer's geometry often hinders hydrogeological investigations. While covering the entire aquifer system with numerous, evenly spaced boreholes could effectively address this issue, the high cost of drilling makes this approach impractical. Instead, remote data collection techniques, such as geophysical geoelectric techniques and remote sensing, offer a more efficient solution by providing precise information about water-bearing formations more quickly and at a lower cost. In order to avoid the common failures associated with wells drilled based on surface geological data (lithology of geological outcrops) and/or findings from nearby boreholes, these techniques are typically utilized

during preliminary investigations for installing new boreholes [1]. These techniques can also be applied to more localized investigations to better understand a hydrogeological system. In this instance, they are frequently used as a supplement to existing boreholes by providing information about unknown water sources. Boreholes alone are generally insufficient to reconstruct an aquifer's geometry in detail [1–3].

In regional hydrogeological research, geophysical prospecting and satellite image processing are usually treated separately [1,4–11], despite the fact that these two techniques work better together. However, the preliminary phase of any geophysical study should incorporate a remote sensing survey [1]. Remote sensing provides information over vast areas and offers spatiotemporal resolutions that facilitate comprehension of the evolution of various environmental components. Hence, it can serve as a guide for making crucial choices such as selecting the geophysical techniques to be used (e.g., seismic refraction, electrical, electromagnetic, and magnetotelluric methods) and the delineation of the areas to be exploited. It is especially helpful in identifying areas of interest for focused geophysical surveys.

Understanding the key mechanisms governing groundwater chemistry is essential, yet challenging, for sustainable groundwater resource management, particularly in complex geological and hydrogeological settings [12]. The quaternary alluvial aquifer is a vital water resource in the Mateur region in the Bizerte region of Tunisia, sustaining local domestic and agricultural water supply [13,14]. The aim of this study is to characterize the geometry of the Mateur aquifer system through an integrated approach using data from boreholes, geophysical methods, and remote sensing. The study seeks to enhance our understanding of the aquifer system's structure and validate these insights with a combination of these techniques.

2. Materials and Methods

2.1. Geographical, Geological, and Hydrogeological Contexts

The Mateur plain has a surface area of about 260 Km^2 and is part of the huge Ichkeul watershed (2600 Km^2) in the Bizerte region of northern Tunisia (Figure 1). The region under study has a Mediterranean sub-humid climate with a significant variation in mean monthly temperatures. The coldest month is January, with a mean temperature of 11 °C, and the hottest month is August, with a mean temperature of 27 °C. The area's potential evapotranspiration values are around 1800 mm/year, while the mean annual precipitation is 570 mm.

The Mateur plain is characterized by lithostratigraphic units ranging in age from the Triassic to the Quaternary (Figure 2). The carbonate formations that define the Tertiary deposits of the Ichkeul Mountains make up the majority of the stratigraphic succession. In the Mateur plain, only the three Campanian hills of Sidi Mbarek, Mateur, and Ras El Ain contain outcrops older than the Quaternary period [15].

Due to the variety in the textural and structural features of the alluvial beds, a multilayered aquifer system, including both confined and unconfined aquifers, is present within these alluvium deposits. This alluvial aquifer, composed of Quaternary formations unevenly arranged on top of the Miocene sediments (Mateur–Ras E Ain), contains alluvial (sand and gravel), eolian (fine-grained sand), and minor lacustrine (sandy clay) deposits. Additionally, there is a deep confined aquifer containing limestone, marl, and clay. The interconnection of the alluvial and limestone aquifers forms a single hydrogeological unit [16]. The groundwater samples of this study were taken from alluvial aquifers at a depth of a few tens of meters. Rainfall infiltration and river leakage (in Joumine, Tine, Sejnane, Melah, and Rezala) are the primary sources of groundwater replenishment. Water levels in 20 water supply wells were measured to calculate the groundwater flow in the Mateur aquifer (Figure 3). In the upstream portion of the plain, groundwater flow is generally directed in the south-north and southeast-northwest directions, while in the downstream portion, it is greatly influenced by the Joumine River's draining activity.

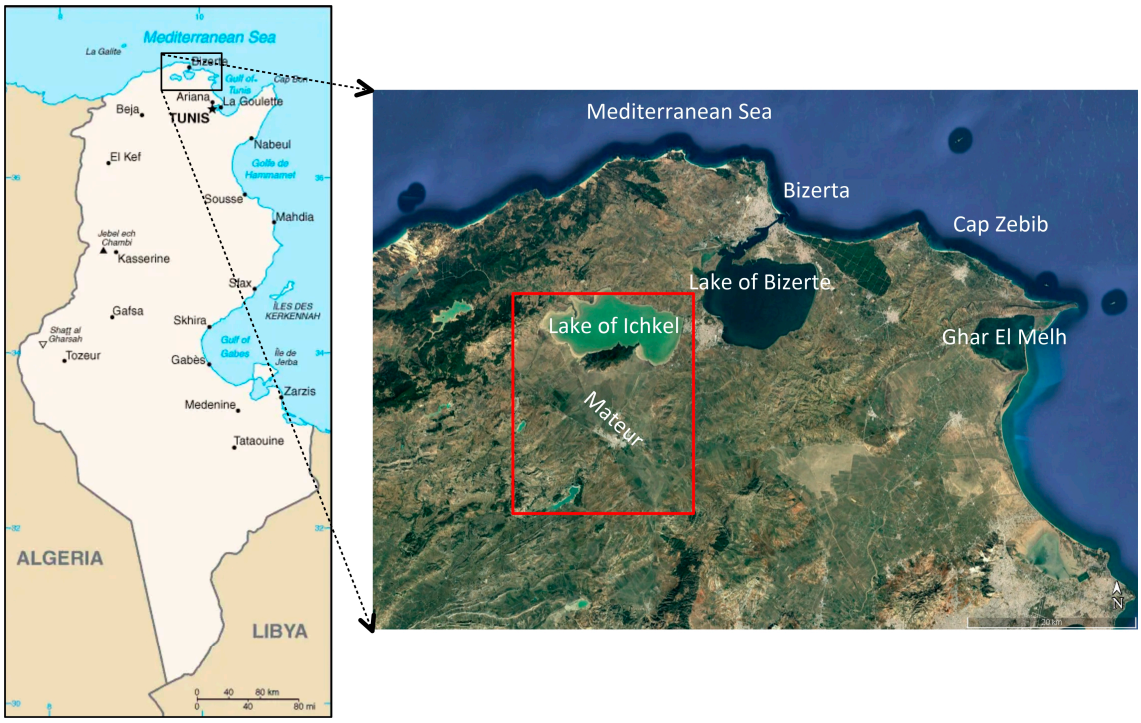

Figure 1. A map showing the location of the Mateur plain (red rectangle). Image © 2024 Airbus. Used in accordance with the Google Maps/Earth terms of service for research purposes.

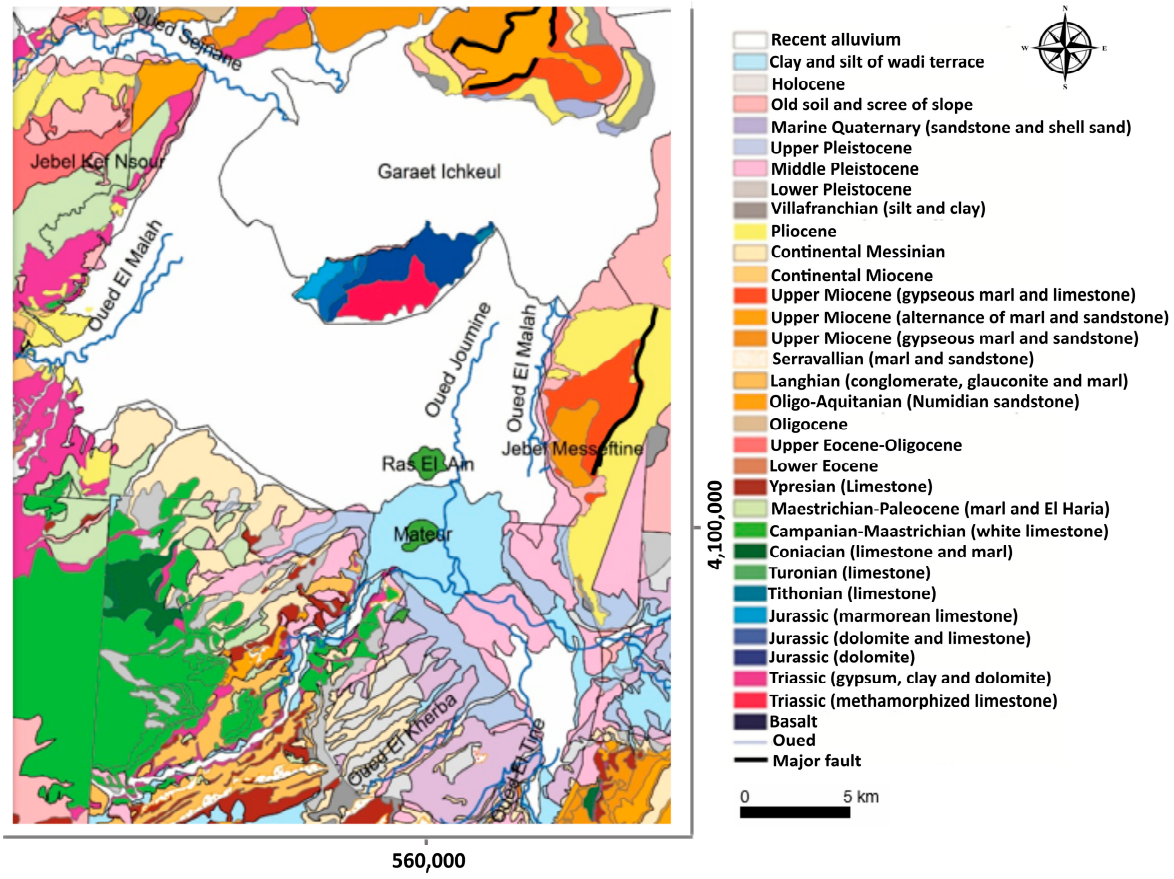

Figure 2. Geological map of the study area.

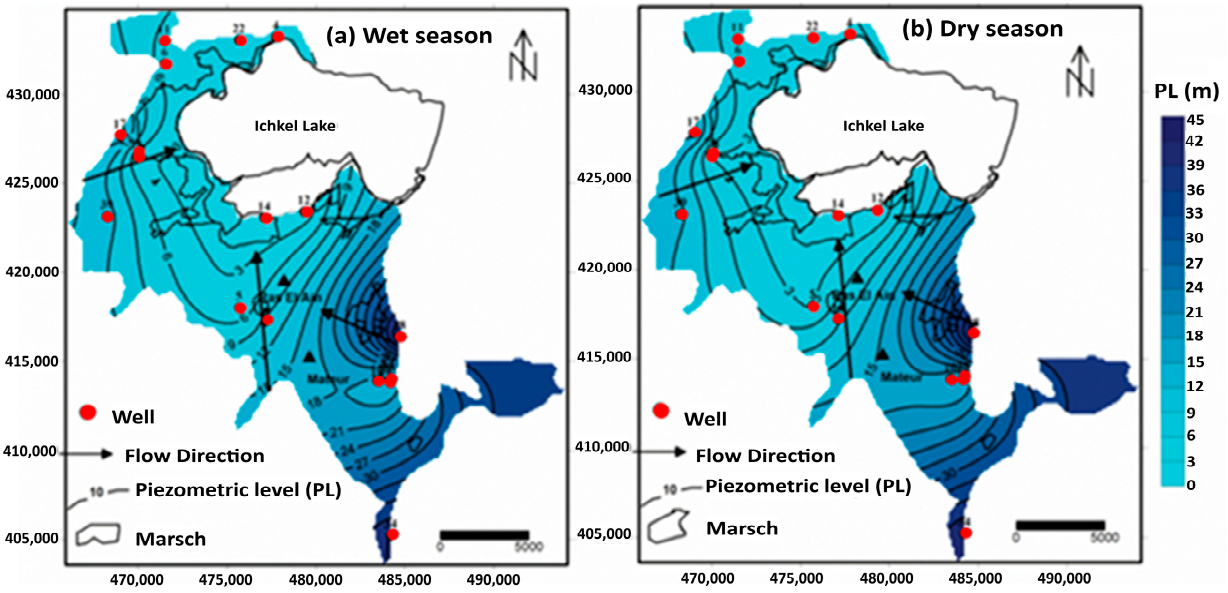

Figure 3. Piezometric maps of Mateur plain: (**a**) wet season; (**b**) dry season. The piezometric levels are higher during the wet season compared to the dry season.

Water is lost from the aquifer through discharge to Lake Ichkeul, pumping for irrigation, and direct evaporation in regions with a low hydraulic gradient and poor permeability [16]. Since the water table often lies 8 to 10 m below the ground surface, evapotranspiration contributes to further groundwater loss. The topography of the area includes lower to medium slopes, where the vegetation primarily consists of Hypericum crispum, Convolvulus arvensis, Papaver rhoeas, and Ridolfia segetum, though it is not well-developed. As the slope increases towards the middle and upper sections, the vegetation changes slightly, with the presence of Arisarum vulgare and Ridolfia segetum, which also remain underdeveloped. In areas of medium slope, the dominant vegetation includes Hypericum crispum and Papaver rhoeas. The agronomic regime in these regions focuses on cereal crops, particularly wheat [17]. The alluvial and the limestone aquifers have transmissivity ranges of 0 to 60 $\times$ 10^{-4} m^2/s and 60 to 320 $\times$ 10^{-4} m^2/s, respectively. Groundwater from the Mateur alluvial aquifer is used for domestic and agricultural purposes [16].

2.2. Data and Methods Used

This study used a multitude of prospecting techniques and data sources, including remote sensing image processing, VES, and the analysis of well logging from the available water boreholes.

2.2.1. Satellite Imagery

Remote sensing satellite imagery refers to the collection of earth surface data by recording reflected electromagnetic energy using satellites (e.g., Sentinel-2, Landsat, PlanetScope) [18]. The resultant image is a digitally structured image composed of pixels, each assigned with a value corresponding to the radiation reflected by the observed object [19].

The European Space Agency (ESA) launched two satellites (S-2A and S-2B) in 2015 and 2017 for the Sentinel-2 mission, comprising the second environmental monitoring plan for the Copernicus mission. The multi-spectral instrument (MSI) sensor embedded in both satellites provides a spatial resolution of 10–60 m, depending on band wavelength. The Sentinel-2 mission offers open access to image data for the global land surface with a six-day revisit period [20]. For the current study, Sentinel-2 (L1C) data were used. The satellite image utilized in this research was taken by Sentinel-2 during the summer period, characterized by clear skies, which ensured good sensor visibility. Various corrections, including atmospheric, geometric, and radiometric corrections, were applied to the satellite

imagery: the digital number (DN) was converted first to radiance and then to reflectance, corresponding to the radiometric correction. Additionally, the atmospheric correction was applied to Sentinel-2 images. Numerous ground control points and polynomial adjustments were applied. The darkest pixel (DP) method, a prompt and precise atmospheric correction technique, was applied using dark and non-variant targets detected in satellite images [20].

2.2.2. Water Boreholes

The "Bizerte Regional Commissariat of Agricultural Development" provided information on 19 water boreholes: F1 to F5 were situated in the northwest at the level of Sejnane; F6 to F11 were located near Ras El Ain; F12 to F17 were installed in Mateur; and single boreholes, F18, at Oued Kherba, and F19 at Oued Tine (Figure 4). These boreholes include lithological columns, gamma ray (GR), and resistivity wireline loggings, among others (measured after drilling). The natural radioactivity of the rocks in a borehole is measured using GR logging [21–23]. The primary radioactive elements, including potassium (^{40}K), uranium (^{238}U and ^{235}U), and thorium (^{232}Th and ^{230}Th), are concentrated in shales with high GR readings up to 200 API [24,25]. Conversely, the GR responses of reservoir rocks such as sandstone, sand, gravel, and carbonate are minimal (typically less than 40 API) [26]. As a result, the GR log is effective at differentiating between clays and permeable formations.

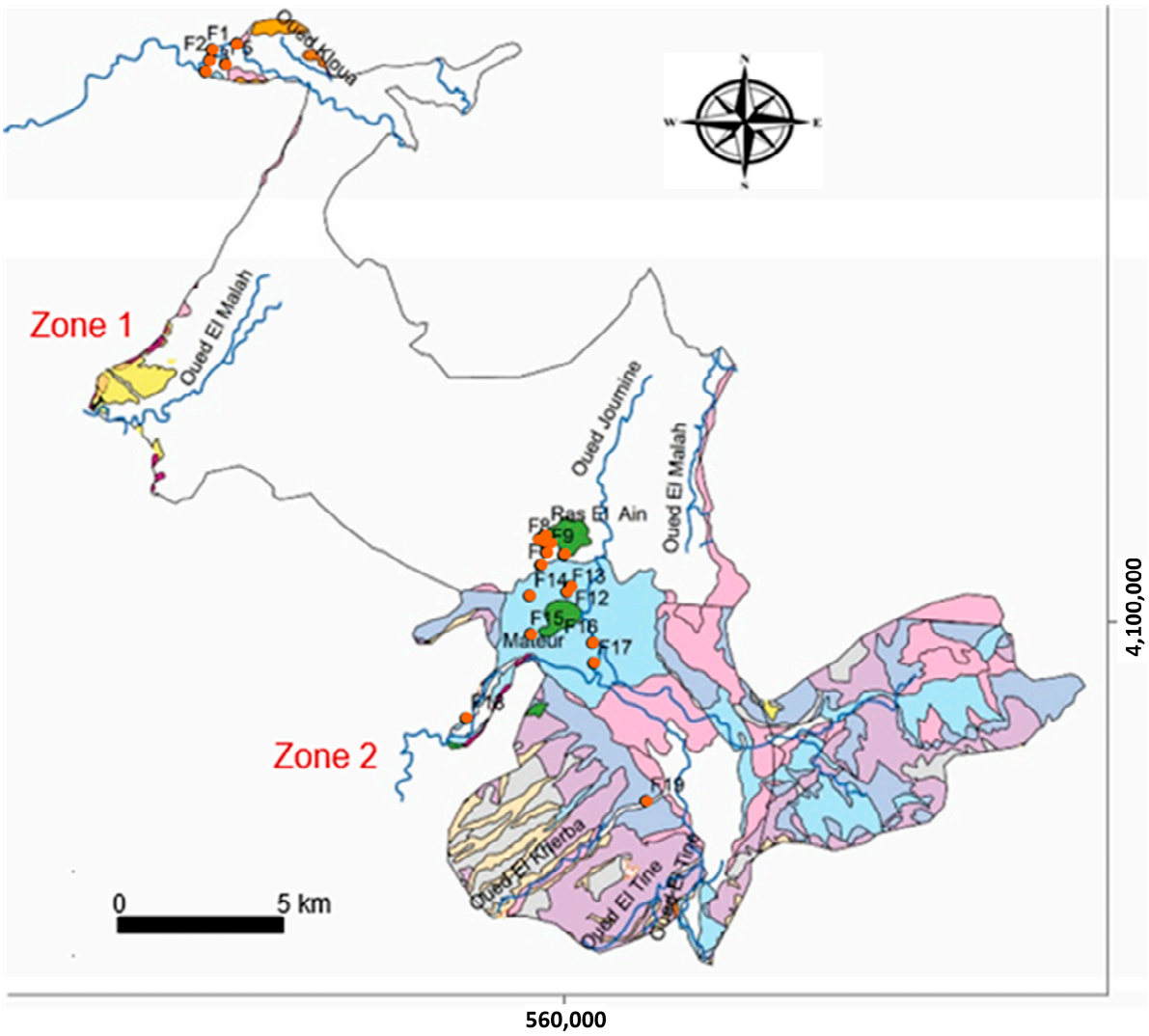

Figure 4. A map showing the locations of the water boreholes (F1 to F19) in the survey area superimposed on the geological map in Figure 2. The boreholes are represented by orange dots.

Short and long standard sondes were used to record the resistivity logs. The short normal sonde, often known as the 16-inch normal, shows the flushed zone's resistivity (Rx0). The 64-inch-long standard sonde offers greater depth of penetration. It provides values comparing the invaded zone's (Ri) and uninvaded zone's (Rt) responses [24]. These low values for clays might vary greatly for reservoir strata depending on the salinity of the ingested water. In contrast to brine water, fresh water is typically resistive [24,27,28].

2.2.3. VES Survey

The VES data utilized in this study were acquired by the General Geosciences Services at 69 locations using the Schlumberger array during the summer. Specifically, 11 VES stations were acquired near Oued El Melah, 4 VES stations near Oued Joumine, and 54 VES close to Oued Tine (Figure 5). The maximum spacing of current electrodes (AB) was 400 m for most of the VES stations, but at some stations, it extended to 600 m.

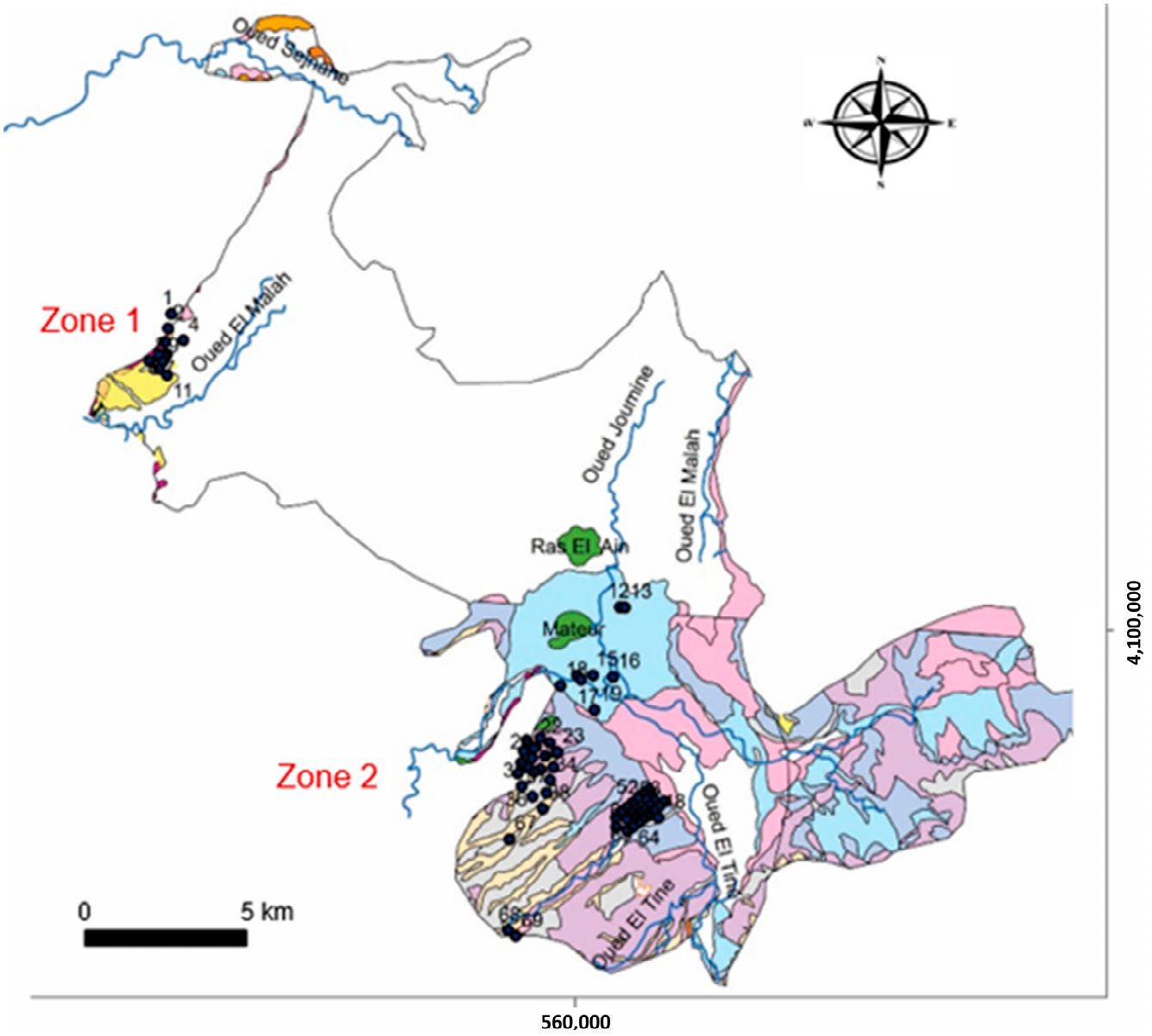

Figure 5. Distribution of VES stations superimposed on the geological map of Figure 2, with stations marked by black dots.

VES is the most popular electrical technique for measuring resistivity to extract information about the subsurface, particularly for hydrogeological purposes [27,29]. Resistivity, denoted as ρ and measured in Ohm·m, is a material's ability to resist electric current. It varies greatly from one material to another since it is affected by a variety of parameters, including rock type, porosity, pores conductivity, water saturation, water salinity, and metallic content [29–31]. For instance, pyrrhotite (FeS) is constantly very conductive and has a resistivity of about 10^{-5} Ohm·m, whereas igneous and metamorphic rocks often have high resistivity values (10^3 to 10^6 Ohm·m). Groundwater, which serves as an electrolyte, significantly influences the electrical conductivity of sedimentary rocks like the Mateur Quaternary deposits by reducing the resistivity values [32]. The concentration and mobility of ions have an impact on the conductivity of groundwater. Mobility varies from ion to ion and rises with temperature (e.g., H^+ has a velocity of 36.2×10^{-8} m/s compared to Na^+ of 5.2×10^{-8} m/s) [33].

In order to evaluate resistivity, two current electrodes (A and B) are often used to transmit the electrical current into the ground. The potential difference between the other two potential electrodes (M and N) is then measured. The following equation is used to determine the apparent resistivity (ρ_a) [34]:

$$\rho_a = K\frac{\Delta V}{I}$$

where I is the current injected into the ground via current electrodes (A and B), ΔV is the potential difference between the potential electrodes (M and N), and K is a geometric factor depending on the electrodes array.

The Wenner, Schlumberger, and dipole-dipole arrays are among the most popular configurations for resistivity measurements, each utilizing four electrodes arranged and spaced differently. In this study, the Schlumberger array was employed, featuring a symmetric arrangement of the four electrodes. In this design, the potential electrodes (M and N) are placed much closer together than the current electrodes (A and B), where AB >> MN. This configuration is widely used for VES to monitor changes in resistivity with depth below the center of the array [35,36]. To enhance the penetration depth of the current lines, the potential electrodes M and N are shifted incrementally during the measurement process.

2.2.4. Integration of Methods

Figure 6 illustrates the hierarchical structure of this study. To accurately analyze the lithological columns from the drill cuttings, the well logs were initially carefully reviewed. They provide accurate information about the location and composition of the reservoir rocks [37–40]. Due to their high permeability, which can exceed 10^{-1} m/s [41] for gravel and sand, the coarse components of the Mateur Quaternary alluvia serve as significant water reservoirs.

To assist the correlation between VES calibration and water boreholes, we extracted different layer units within the lithological columns, mainly clay units and predominantly coarse units. The majority of the clay unit intervals have low resistivity and high radioactivity, while the coarse ones exhibit the opposite characteristics. These latter units contain the greatest amount of Mateur groundwater and are designated as reservoir formations or reservoir units.

Second, the configuration of the Mateur aquifer system was reconstructed using qualitative and quantitative interpretation of the VES stations. Maps of apparent resistivity at various AB spacings were established, providing a qualitative depiction of the resistivity distribution at various depths to gain insight into the potential locations of water reservoirs.

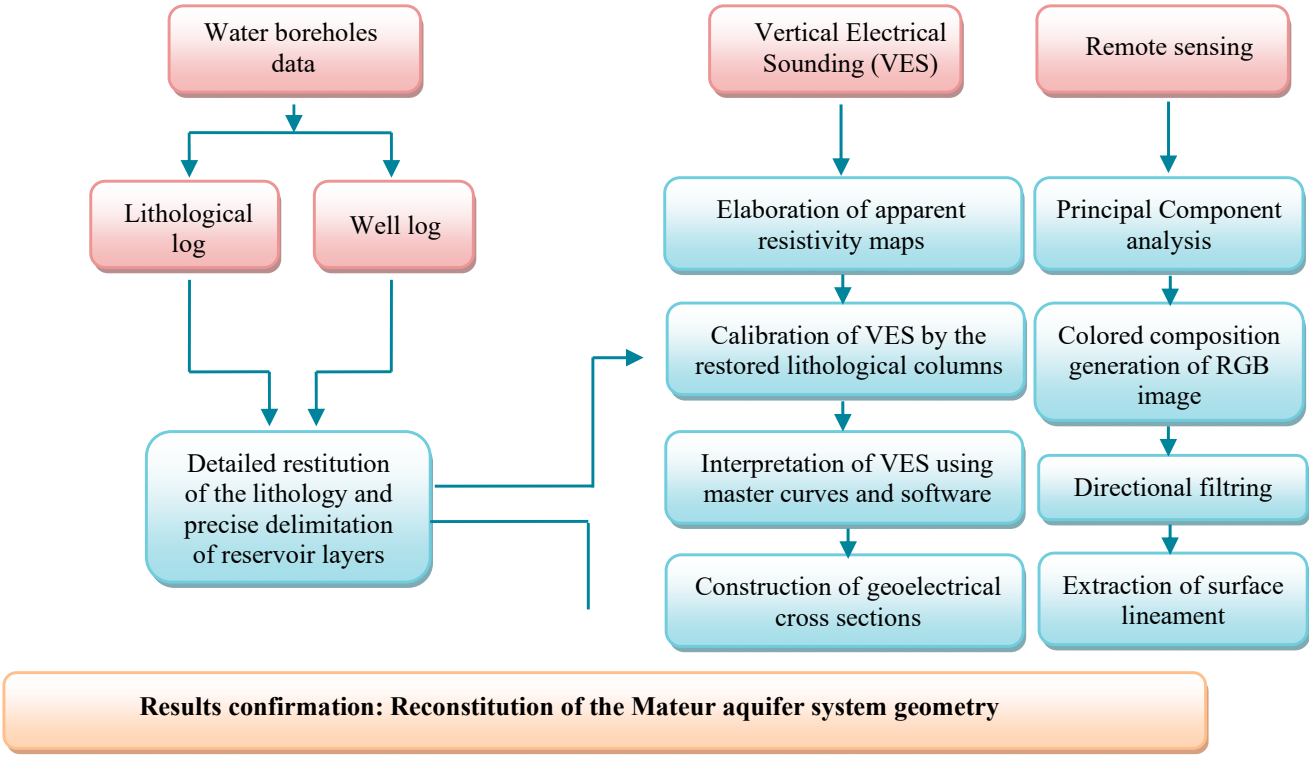

Figure 6. Flow chart diagram of the used methodological hierarchical structure.

The first step in quantitative interpretation was VES calibration, which involved comparing the lithological columns with the proximal VES curves to relate each Quaternary lithological unit to its resistivity. The relationships obtained were established by comparing the VES curves to the theoretical master curves of Orellana and Mooney [42] and then further refining and inverting them using IP2WIN v. 2.1 software. This process guided our interpretation of the remaining electrical data. The outcome was obtained by superimposing the experimental and theoretical curves. The models inferred from the VES interpretation—layer thicknesses and true resistivities of each identified layer—were correlated with the lithological logs in the form of geoelectrical cross-sections, whose analysis clarifies the aquifer geometry [43,44].

The final phase involved processing the satellite image to support the VES findings. To extract the surface lineaments, which may correspond to tectonic features influencing the aquifer structure, methods such as principal component analysis (PCA), color composition (Figure 7), and directional filtering were employed. Directional filtering, in particular, is an image-processing technique that enhances linear features in a specific direction while suppressing those in other directions. This is achieved by applying filters that are sensitive to edges or contrasts in a given orientation. A set of convolution kernels (small matrices) is designed to enhance features in specific orientations (e.g., 0°, 45°, 60°, and 90°). Common directional filters include Sobel, Prewitt, and Kirsch filters [45–49].

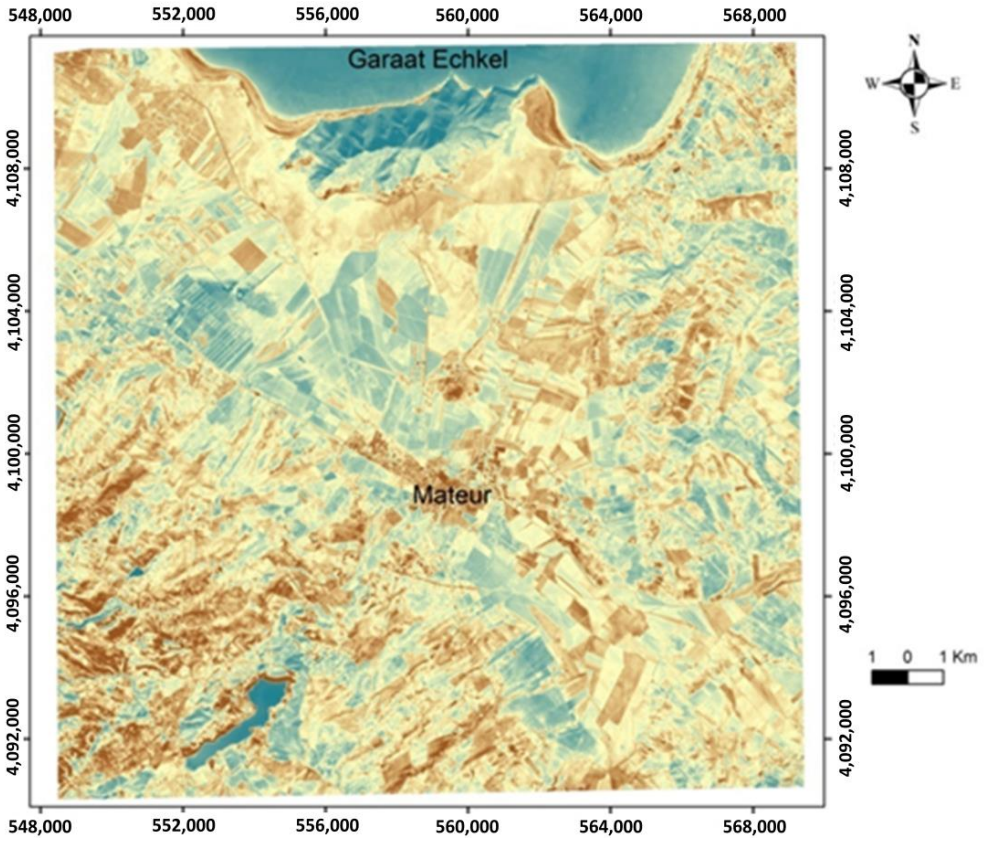

Figure 7. Realized RGB image (color composite) of the study area.

3. Results and Discussion

The analysis of well logs has identified a multi-layer aquifer composed of alluvial and limestone deposits. Five water boreholes are located in the southern part of the plain. Boreholes F7, F10, and F11 access the deep Ras El Ain aquifer, while F12 and F14 exploit water from the Mateur groundwater aquifer. To clearly illustrate the contribution of diagraphies, we compared the available lithological logs with the interpreted ones. The multi-layers that comprise the alluvial aquifer consist of alluvial, aeolian, and small lacustrine deposits [15,16]. The limestone aquifer, the main productive layer, corresponds to the Abiod Formation, dated to the Campanian–Maastrichtian age.

The examination of the available lithological column for the old drilling F7 (illustrated at the left of Figure 8, selected as an example), represents three reservoirs. The first one extends from 14 to 17 m, corresponding to pebbles and clay soils. The second spans from 27 to 70 m, and the third, which ranges from 83 to 106 m, is composed of limestone soils. However, the lithological log illustrated at the right of the figure, obtained from updated diagraphic recordings for both spontaneous polarization (SP) and resistivity, indicates five reservoirs: [14 to 18 m] and [19 to 23 m], corresponding to resistivity values between 50 and 90 Ohm·m, assigned to pebbly and clayey lithology; [65 to 70 m] and [72 to 76 m], with a resistivity values ranging from 40 to 98 Ohm·m; and the last one [94 to 106 m], consisting of limestone lithology. In order to achieve greater accuracy, this study will rely on the interpretation of the well log. Three types of resistivity were measured: shallow resistivity (short normal, SN), which represents the resistivity of the invaded zone; deep resistivity (long normal, LN), which represents the resistivity of the uninvaded zone; and inversed resistivity (INV), which is compared with a reference point at the surface. The numbers in the heading indicate the diameter of the penetrated zone measured, in inches.

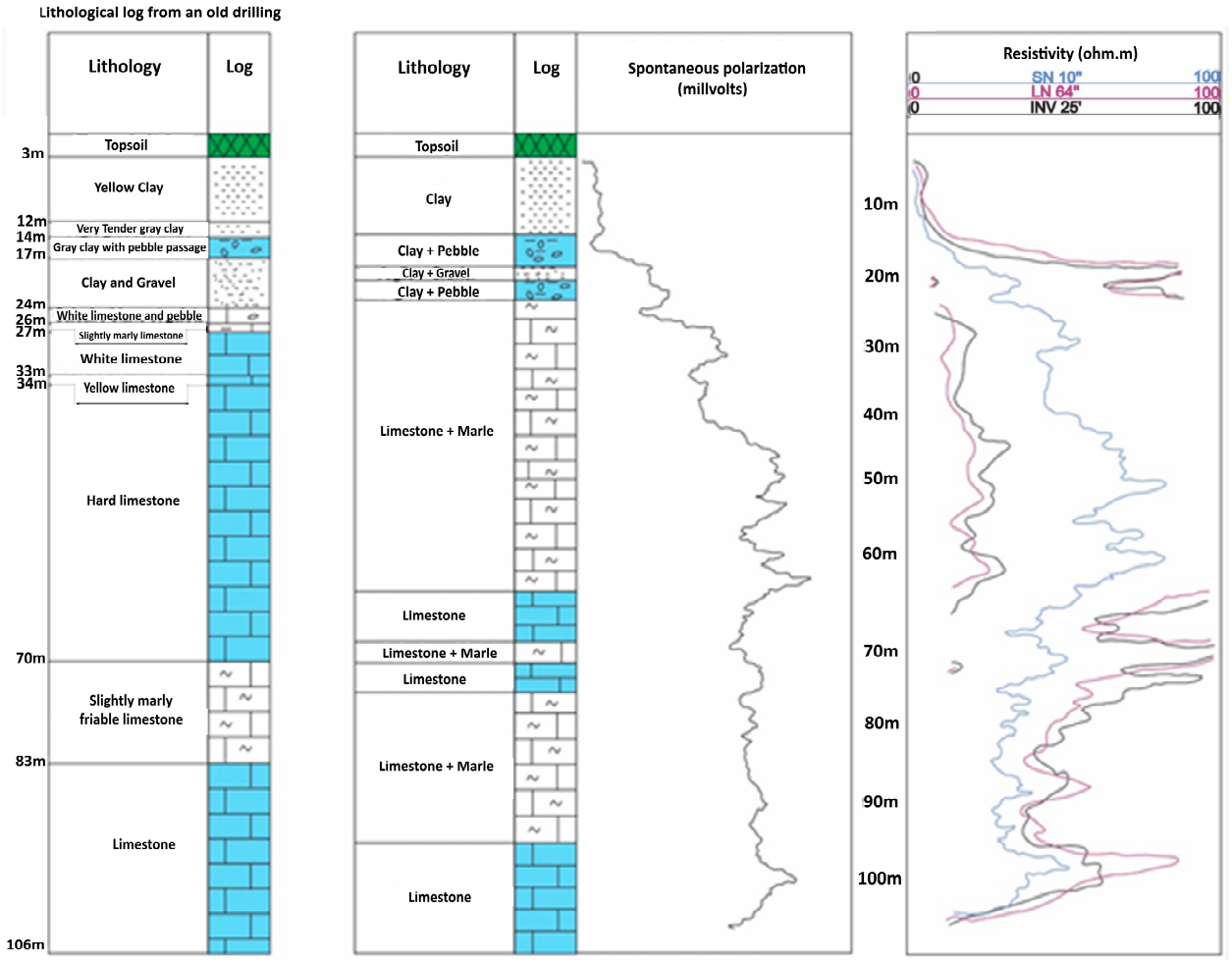

Figure 8. Borehole F7 lithological column and well logs including SP and resistivity. The left lithology log was obtained from an old log description whereas the one on the right was extracted from an updated well log.

The lithological column for borehole F10, with a depth of 50 m, reveals a single reservoir extending from 8 to 64 m, composed of limestone. Resistivity logs identified two distinct zones: one between 15 and 22 m with resistivity values varying between 30 and 98 Ohm·m, and another from 45 to 58 m with resistivity values between 40 and 98 Ohm·m.

For borehole F11, which has a depth of 90 m, the lithological log reveals two permeable layers composed of limestone, pebbles, and gravel. These layers are located at depths of 31–37 m and 51–90 m. The resistivity recording highlights the presence of two potential water-bearing zones, corresponding to the intervals of 26–37 m with resistivity values of 20–80 Ohm·m, and 50–58 m with resistivity values of 25–97 Ohm·m.

The lithological column for borehole F12, which taps into the Oued El Tine aquifer with a depth of 163 m, primarily shows clay deposits. Two reservoir units composed of clay and pebbles are present at depths of 17–40 m and 47–58 m. The resistivity recordings highlight two layers rich in coarse sediments corresponding to the intervals 26–37 m and 50–58 m. The geoelectrical log shows the highest resistivity values, ranging from 50 to 97 Ohm·m for the 26–37 m interval and 60–97 Ohm·m for the 50–58 m interval. The poor quality of the Oued El Tine's aquifer, with water salinity measuring 2.8 g/L, explains these relatively low resistivity values, which are associated with clayey and marl soils, leading to low permeability and thus low productivity.

The lithological column of the borehole F14, with a depth of 161 m, reveals two layers rich in coarse sediments at depth ranges of 7–32 m and 47–50 m. The resistivity recordings highlight five zones potentially suitable as water reservoirs, corresponding to the intervals 53–67 m, 80–86 m, 92–102 m, 103–111 m, and 122–131 m, with resistivity values ranging from 10 to 99 Ohm·m.

Based on the lithological columns, we can conclude that the Ras El Ain (boreholes F7, F10, and F11) represents a reservoir with a thickness of 20–55 m, while the plain of Oued El Tine (boreholes F12 and F14) contains a multi-layer aquifer with several reservoirs with a thickness of 10 to 20 m.

Twelve apparent resistivity maps were established for different AB spacings. To facilitate the analysis, zone 1 was assigned to the north part of the Mateur plain, where the Oued El Melah is located, while zone 2 corresponds to the south part of the plain of Mateur (refer to Figure 5). For the short distance of AB/2 = 3 m, which corresponds to the superficial layers, relatively high apparent resistivity values were observed with approximately 170 Ohm·m in zone 1 at and around 130 Ohm·m in zone 2. However, for the AB/2 = 4 m distance map (Figure 9), the resistivity decreased to 90 Ohm·m in zone 1 and 95 Ohm·m in zone 2.

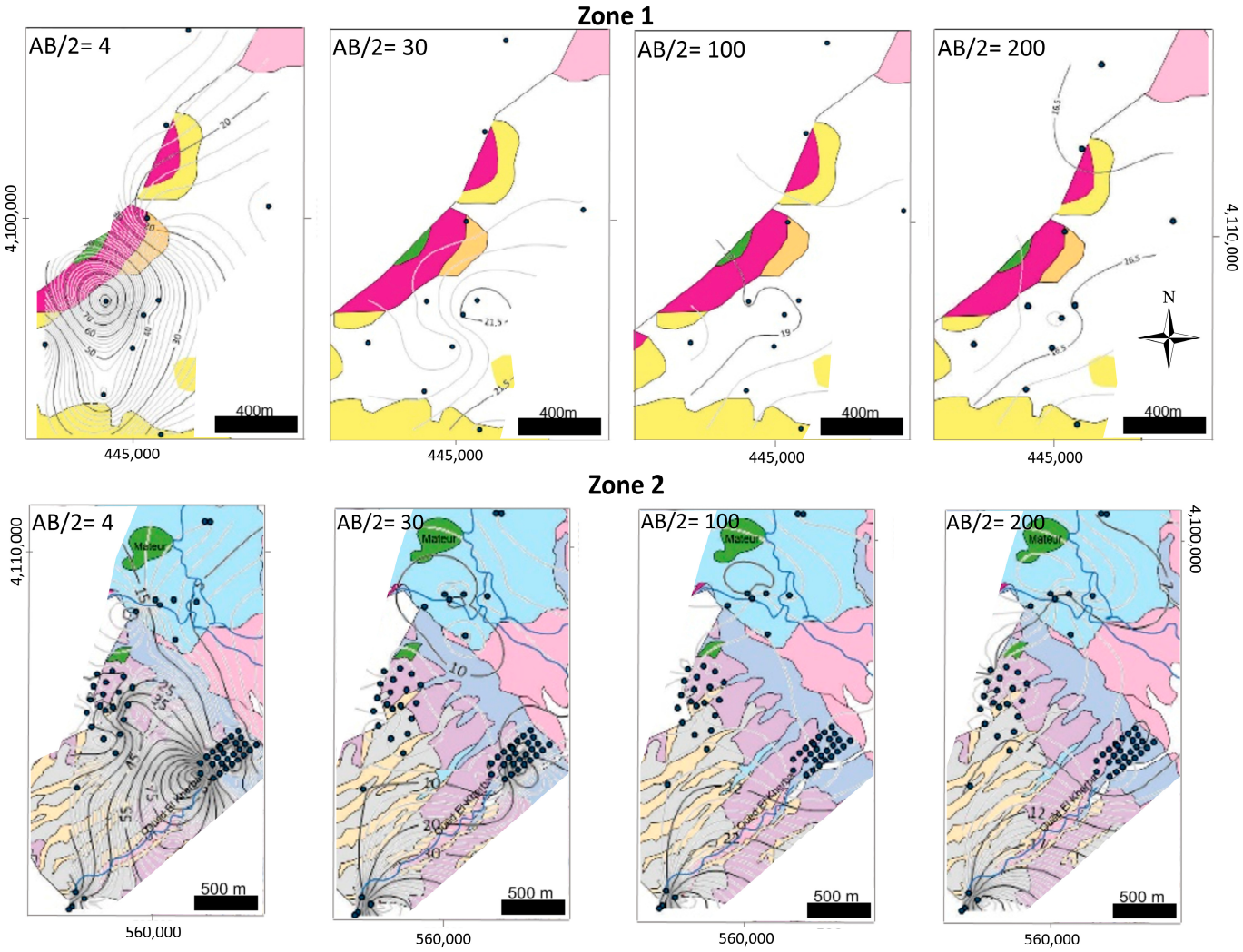

Figure 9. Apparent resistivity maps for zones 1 (upper panel) and 2 (lower panel) are presented for different depth slices corresponding to AB/2 spacings of 4 m, 30 m, 100 m, and 200 m.

For larger AB/2 spacings of 10 m, 15 m, 20 m, 30 m, 40 m, 50 m, 100 m, and 150 m, the high apparent resistivity values displayed a consistent spatial distribution across both zones.

In zone 1 (Oued El Melah), resistivity remained constant at 20–25 Ohm·m, while in zone 2, the resistivity distribution was divided, with values of 25–40 Ohm·m in the west-east part and 45–55 Ohm·m in the southwest part. These distinctions are particularly evident in the maps for AB/2 = 30 m and AB/2 = 100 m, which are presented as examples (Figure 9).

The maps for AB/2 spacing of 200 m and 300 m show that the resistivity values are less than 20 Ohm·m across the entire study area, indicating predominantly clay soils. In zone 1, the highest measured value was 16 Ohm·m in the northwest part, while in zone 2, it reached 25 Ohm·m. The map for AB/2 = 200 m is selected as an example in this paper (Figure 9).

The VES calibration was accomplished by means of two boreholes, F17 and F19, located near VES stations 16 and 48, respectively (Figure 10). A comparison between VES16 and the lithological column of borehole F17 (Figure 11) shows that the clayey soil corresponds to a resistivity value of 2.5 Ohm·m, the sandy clay layer to 7 Ohm·m, and the gravel and pebbles layer to a resistivity value of 22.5 Ohm·m. Similarly, the comparison between VES48 and the lithological column of borehole F19 reveals the following: the topsoil has a resistivity value of 18.4 Ohm·m; the sandy layer has a resistivity value of 30.5 Ohm·m; the gravel, pebbles, and gravelly layers have a resistivity value of 20 Ohm·m; and the clay layer has a resistivity of 6.5 Ohm·m.

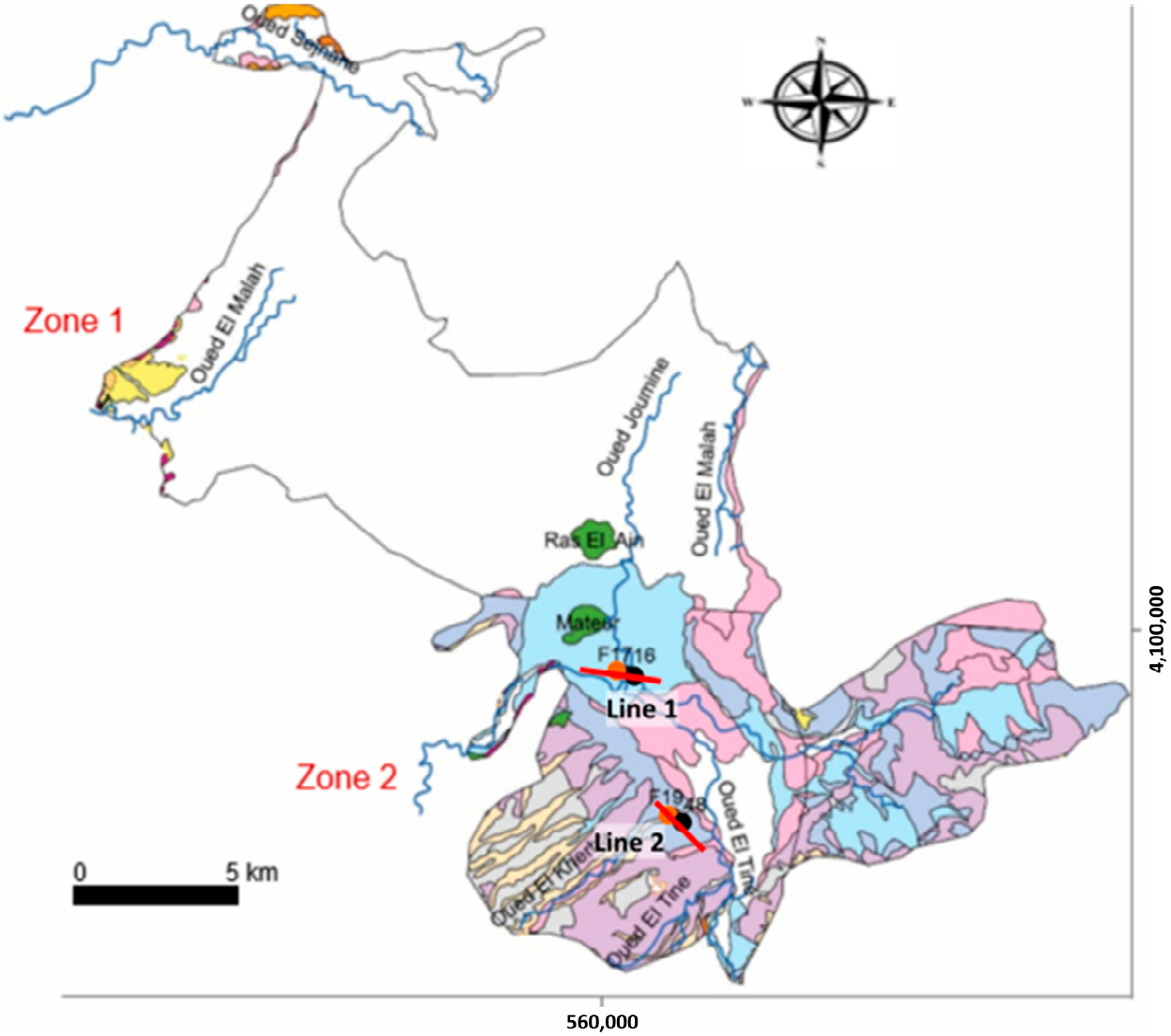

Figure 10. Distribution map of boreholes and the location of the selected profiles presented in this study. Orange dots represent the boreholes, black dots indicate the VES stations, and red lines mark the selected profiles.

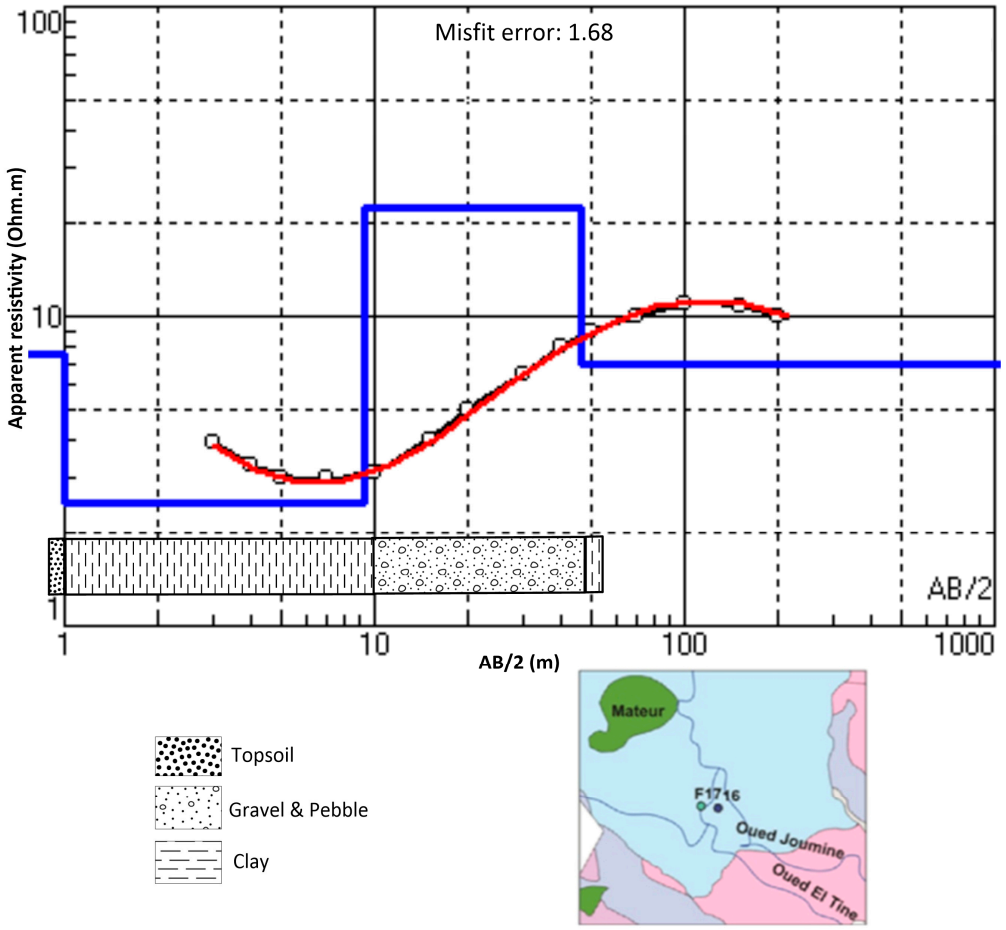

Figure 11. Result of 1D inversion of VES16, along with the calibration using the lithological column from borehole F17. The circles, red line, and blue line represent the measured data, calculated data, and thicknesses and resistivities of the interpreted layers, respectively.

Several geoelectrical cross-sections were established in various directions, and two of them were selected as examples in the present work. Geoelectrical cross-section 1, oriented E–W (Figure 12), runs along Oued El Tine and includes the lithological log of borehole F17, along with three electrical soundings (VESes 14–16). The topsoil has a thickness ranging from 1 to 5 m, with resistivity values between 5.5 and 18 Ohm·m. The second layer, with a thickness of 5 to 9 m, represents clayey soil as inferred from borehole F17, with a resistivity range of 2.5 to 8 Ohm·m. The third layer, extending from 7 m below VES15 to 62 m below VES14, is characterized by pebbly and gravelly lithology, as indicated by borehole F17, and has a resistivity range of 19 to 22.5 Ohm·m, suggesting a good groundwater aquifer. Its thickness increases westward. The fourth layer consists of clay with an average resistivity of around 7 Ohm·m.

The second geoelectrical cross-section (Figure 13), located at the southern edge of the Mateur plain near the Mateur graben, integrates the lithological column from borehole F19 and data from five VES stations (VES 44–48). The first layer, representing the topsoil, varies in thickness from 1 to 3 m and exhibits resistivity values between 12 and 69 Ohm·m. The second layer, identified as sandy, extends to a depth of 14 m below VES48 and has resistivity values ranging from 14.5 to 40.4 Ohm·m. The third layer, consisting of pebbly and gravelly soils, extends to 42 m in depth and decreases in thickness towards the northwest, representing the primary groundwater aquifer in the region. The final layer is clay, with resistivity values ranging from 6.3 to 8.4 Ohm·m.

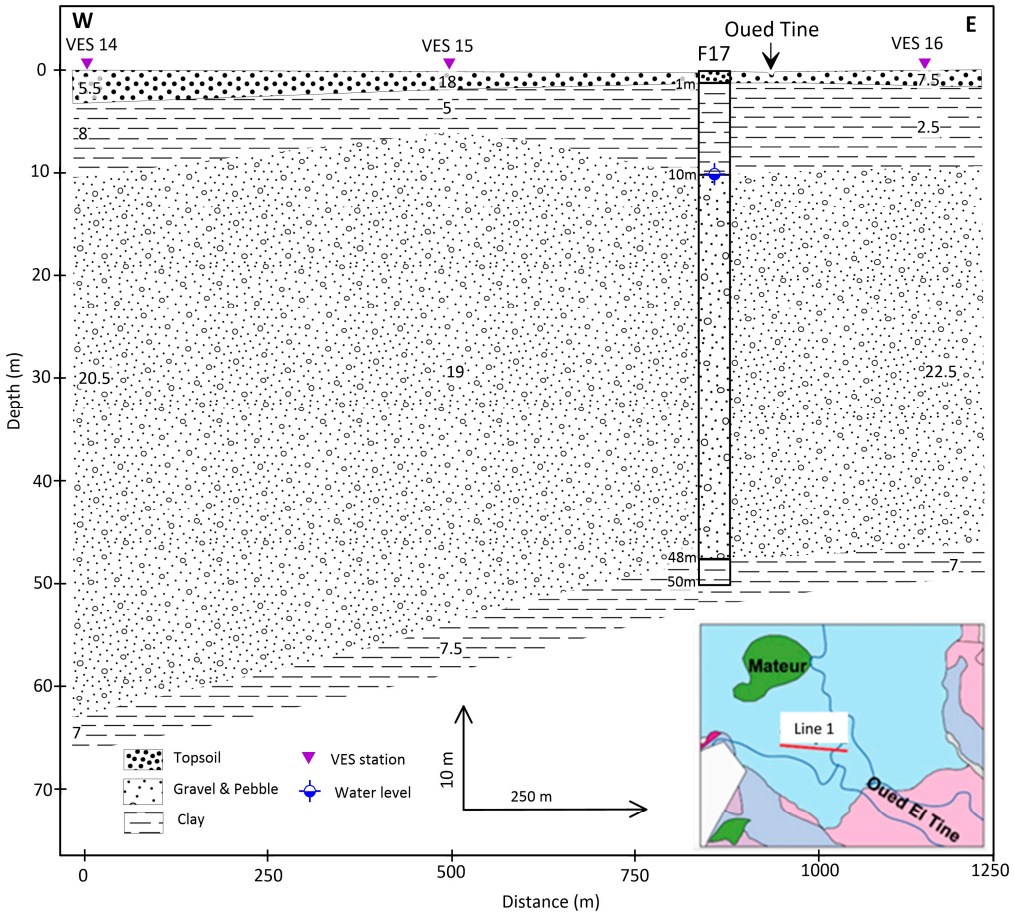

Figure 12. Geoelectrical-geological cross-section 1, obtained from the results of 1D inversion of VES stations VES14, VES15, and VES16 along profile Line 1 (Figure 10) in the plain of Oued Joumine.

Two major faults (Figure 2) run through the region: one in the north-south direction, affecting the western foothills of Messeftine [50], and the other with a complex layout in the northeast-southwest direction, appearing north of Garaet Ichkeul [51]. In this study, the geoelectrical data suggest the presence of several geoelectrical discontinuities which may indicate successive collapses in the southern part of the Mateur plain, possibly influenced by the major Messeftine fault.

Directional filtering was conducted in four directions: N00, N45, N60, and N90 (Figure 14). To create the surface lineaments map, the identified lineaments were then superposed, with those repeated or related to anthropogenic structures (such as high voltage lines and roads) filtered out. The resulting lineaments map, produced from satellite imagery processing, showed 23 lineaments with varying directions in the Mateur plain (Figure 15). Given the minimal variation in plain altitudes, these lineaments are unlikely to be topographical breaks. The tectonic influence on the geometry of the Mateur aquifer is confirmed by a notable coincidence between the discontinuities and the superficial lineaments identified by the geoelectrical cross-sections.

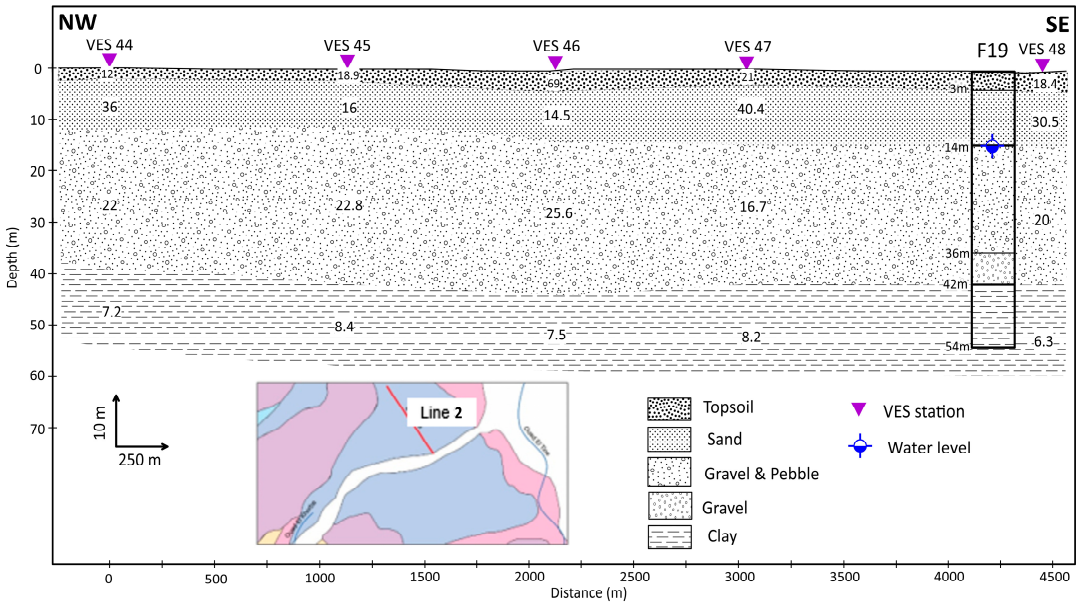

Figure 13. Geoelectrical-geological cross-section 2, obtained from the results of 1D inversion of VES stations VES44, VES45, VES46, VES47, and VES48 along profile Line 2 (Figure 10) in the plain of Oued El Tine.

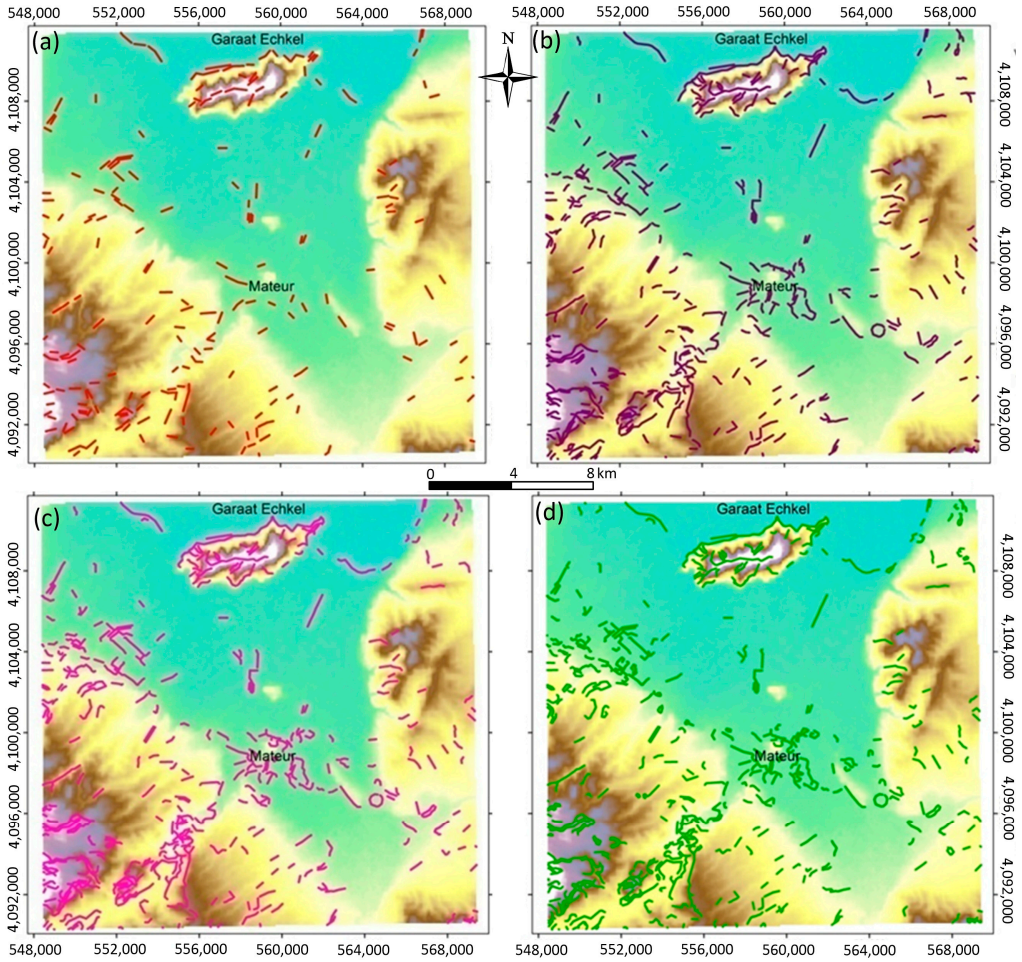

Figure 14. Lineament maps produced by directional filtering with directions of (**a**) N00, (**b**) N45, (**c**) N60 and (**d**) N90.

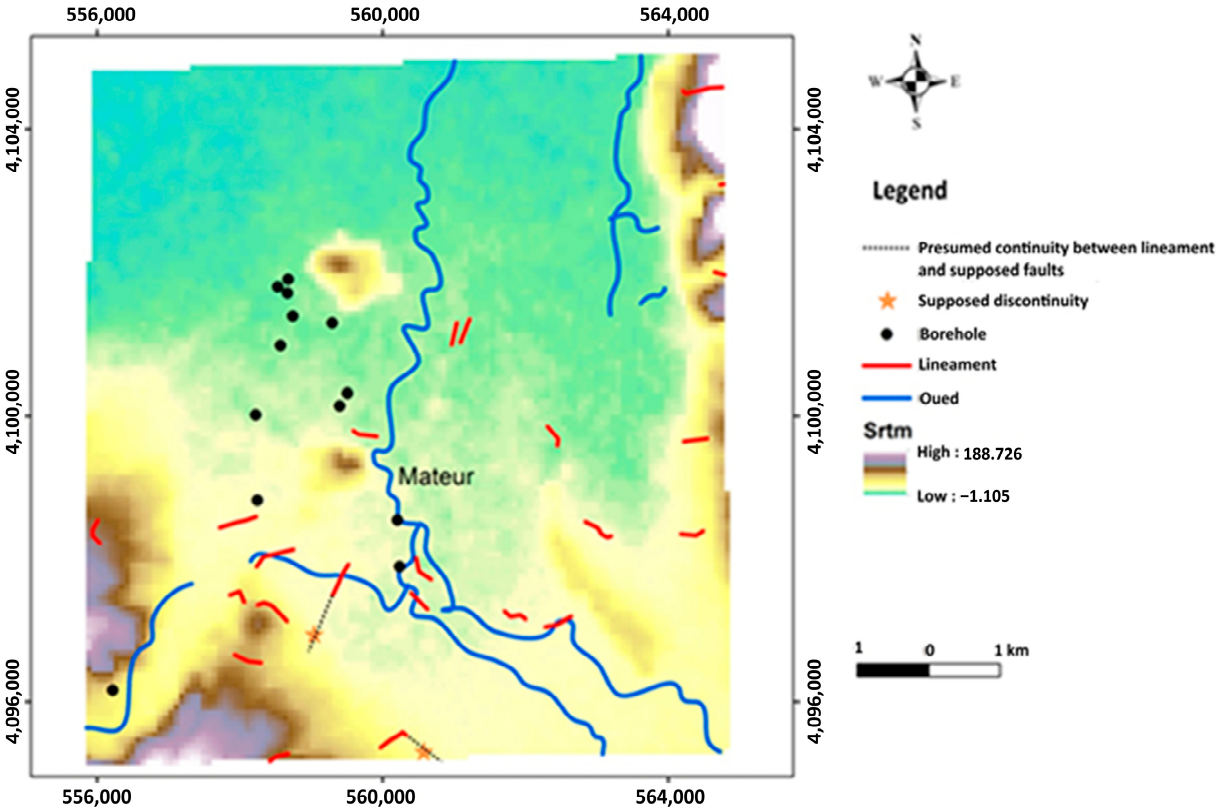

Figure 15. Superficial lineaments discerned from satellite imagery and their correlation with potential discontinuities inferred from geoelectrical cross-sections.

4. Conclusions

The hydrogeological schema of the Mateur plain has been refined through the integrated application of indirect techniques, including VES and remote sensing, along with water borehole data, to characterize the groundwater aquifer in the Mateur region. Additionally, the comparison of the obtained lithological columns with corresponding well logs has effectively identified the Quaternary series.

The processing of satellite imagery, analysis of lithological column, and interpretation of VES data have demonstrated that the geometry of the aquifer in the study area depends on two factors: (1) extensive tectonic activity, and (2) sedimentation mechanisms within the fluvial environment.

The analysis of VES and water borehole data revealed that in the Ras El Ain area, there is a reservoir with a thickness of 20–55 m composed of clay and pebbly gravel limestone lithology, while the plain of Oued El Tine contains a multi-layer aquifer with several sub-reservoirs whose thickness ranges between 10 and 20 m, consisting of clay soils.

This research has provided significant findings that can greatly enhance groundwater analysis in the Mateur region. Furthermore, it can serve as an international reference, demonstrating that geophysical and remote sensing analysis are not only applicable in preliminary studies for water point implantation, but are also powerful tools for characterizing the geometry of alluvial aquifer systems.

Author Contributions: Conceptualization, Wissal Issaoui and Imen Hamdi Nasr; methodology, Wissal Issaoui and Imen Hamdi Nasr; software, Wissal Issaoui and Dhouha Ben Othman; validation, Wissal Issaoui, Imen Hamdi Nasr, Ahmed Ezzine, and Mohamed Hédi Inoubli; formal analysis, Wissal Issaoui, Wafa Bejaoui, and Dhouha Ben Othman; investigation, Wissal Issaoui and Imen Hamdi Nasr; resources, Wissal Issaoui, Imen Hamdi Nasr, Ismael M. Ibraheem, Wafa Bejaoui, and Mohamed Hédi Inoubli; data curation, Wissal Issaoui, Imen Hamdi Nasr, Ahmed Ezzine, and Mohamed Hédi Inoubli; writing—original draft preparation, Wissal Issaoui; writing—review and

editing, Imen Hamdi Nasr, Ismael M. Ibraheem, Dimitrios D. Alexakis, and Mohamed Hédi Inoubli; visualization, Wissal Issaoui, Imen Hamdi Nasr, and Ismael M. Ibraheem; supervision, Imen Hamdi Nasr and Ismael M. Ibraheem; project administration, Imen Hamdi Nasr and Ismael M. Ibraheem; funding acquisition, Wissal Issaoui, Imen Hamdi Nasr, and Dimitrios D. Alexakis. All authors have read and agreed to the published version of the manuscript.

Funding: This research received no external funding. The remote sensing section was added to this project and carried out under the MOBIDOC scheme, funded by the EU through the SWAFY project and managed by the ANPR.

Data Availability Statement: The datasets generated during and/or analyzed during the current study are available from the corresponding author upon reasonable request.

Acknowledgments: The authors express their gratitude to the editor and the reviewers for their thorough evaluation and valuable feedback, which greatly enhanced our paper.

Conflicts of Interest: The authors declare no conflicts of interest.

References

1. Hezzi, M.F.; Guellala, R.; Hamed, F.A.; Ferchichi, Y.; Merzoughi, A.; Inoubli, M.H. Interpretation of geometric elements of the fahs aquifer system, northeast Tunisia: Joint use of vertical electrical sounding data, well logs and satellite imagery. *Nat. Resour. Res.* **2021**, *30*, 321–337. [CrossRef]
2. Alexopoulos, J.D.; Voulgaris, N.; Dilalos, S.; Mitsika, G.S.; Giannopoulos, I.K.; Gkosios, V.; Galanidou, N. A geophysical insight of the lithostratigraphic subsurface of Rodafnidia area (Lesbos Isl., Greece). *AIMS Geosci.* **2023**, *9*, 769–782. [CrossRef]
3. Zarif, F.M.; Elshenawy, A.M.; Barseem, M.S.; Al-Abaseiry, A.A.; Sayed, A.N.E. Evidence of geoelectrical resistivity values on groundwater conditions in Wadi El Natrun and its vicinities, West Delta, Egypt (cases studies). *Sci. Rep.* **2022**, *12*, 10745. [CrossRef]
4. Mitsika, G.S.; Alexopoulos, J.D.; Vassilakis, E.; Dilalos, S.; Poulos, S.E. Investigation of the physical-geographical characteristics of river delta with geophysical and satellite data. The case study of Pineios River, Greece. *MethodsX* **2023**, *10*, 102033. [CrossRef]
5. Youan, T.M.; Lasm, T.; Jourda, J.P.; Kouame, K.F.; Razack, M. Cartographie des accidents géologiques par imagerie satellitaire Landsat-7 ETM + et analyse des réseaux de fractures du socle précambrien de la re´gion de Bondoukou (nord-est de la Côte d'Ivoire). *Télédétection* **2008**, *2*, 119–135.
6. Gnamba, F.M.; Oga, Y.M.S.; Gnangne, T.; Lasm, T.; Bie´mi, J.; Kouakou, Y.K.N. Analyse de la productivité des aquifères de fissures du socle paléoprotérozoïque de la région de Katiola (centre-nord de la Côte d'Ivoire). *Eur. Sci. J.* **2014**, *10*, 79–98.
7. Ben Lasmar, R.; Guellala, R.; Zouhri, L.; Sarsar Naouali, B.; Garrach, M.; Inoubli, M.H. Etude hydrogéologique des séries triasiques dans la région de Jeffara-Dahar (Sud Tunisien): Apport des diagraphies et de la sismique réflexion. *Estud. Geológicos* **2016**, *72*, e044. [CrossRef]
8. Guellala, R.; Amiri, A.; Ben Lasmar, R.; Hamed Ferjeni, A.; Jaouadi, I.; Inoubli, M.H.; Ben Youssef, M. Geophysical contributions to hydrogeological study in the Chemtou-Sidi Miskine Agricultural Sector (Northwestern Tunisia). *Nat. Resour. Res.* **2017**, *27*, 41–50. [CrossRef]
9. Hamed Ferjani, A.; Guellala, R.; Amiri, A.; Merzougui, A.; Ben M'barek, F.; Inoubli, M.H. Structuration profonde dans la re´gion de Bir M_Chergua (Nord-Est de la Tunisie). *Estud. Geológicos* **2018**, *74*, e075. [CrossRef]
10. Idoudi, M.; Guellala, R.; Ben Lasmar, R.; Hamdi, I. Contribution des données de forages d_eau et des sondages électriques verticaux à la caracté risation du système aquifère dans la région de Tataouine (Sud-Est de la Tunisie). In Proceedings of the 8ème Colloque Maghrébin de Géophysique Appliqué e, Hammamet, Tunisia, 21–23 March 2019.
11. Issaoui, W.; Hamdi Nasr, I.; Khaskhoussi, S.; Inoubli, M.H. Monitoring of soil contamination from olive mill wastewater (OMW) using physico-chemical, geotechnical analysis and electrical resistivity tomography (ERT) investigation. *Environ. Earth Sci.* **2023**, *82*, 331. [CrossRef]
12. Issaoui, W.; Nasr, I.H.; Guellala, R.; Hallal, N.; Hamai, L.; Inoubli, M.H. Geophysical contribution based on vertical electrical sounding to hydrogeological evaluation in Ras Jebel coastal aquifer, Tunisia. *Geophys. Prospect.* **2024**, *72*, 1–16. [CrossRef]
13. Jendoubi, A.; Bouhlila, R. Modelling of nitrate transport in the Mateur aquifer (Tunisia). In *Impact of Human Activity on Groundwater Dynamics. Proceedings of a Symposium Held during the Sixth IAHS Scientific Assembly, Maastricht, The Netherlands, 18-27 July 2001*; IAHS Publication, 2001; p. 269. Available online: https://iahs.info/ (accessed on 17 July 2024).
14. Nasri, N.; Chebil, M.; Guellouz, L.; Bouhlila, R.; Maslouhi, A.; Ibnoussina, M. Modelling non point source pollution by nitrate of soil in the Mateur plain, Northeast of Tunisia. *Arab. J. Geosci.* **2014**, *8*, 1057–1075. [CrossRef]
15. Ennabli, M. Contribution à l'étudeHydrologique de la Plaine de Mateur. Ph.D. Thesis, Faculty of Sciences of Paris, Paris, France, 1967.
16. Ennabli, M. Hydrogéologie de la plaine de Ras Djebel –Raf Raf, livre jubilaire M. *Solignac Ann. Mines La Géologie Tunis* **1973**, *26*, 537–561.
17. Mori, A. Etude Pédologique de la Plaine de Mateur (Oued Tine), Secretariat d'Etat à l'Agriculture. Séction Spéciale D'études de Pédologie et D'hydrologie. 1963. Available online: https://horizon.documentation.ird.fr/exl-doc/pleins_textes/divers16-02/10881.pdf (accessed on 11 September 2024).

18. Bonn, F.; Rochon, G. *Précis de Télédétection, (1), Principes & Méthodes*; Presses de l_Université du Québec: Quebec, QC, Canada, 1993.
19. Vani, K. Satellite image processing. In Proceedings of the Fourth International Conference on Signal Processing, Communication and Networking (ICSCN), Chennai, India, 16–18 March 2017.
20. Issaoui, W.; Alexakis, D.D.; Hamdi, N.I.; Argyriou, A.V.; Alevizos, E.; Papadopoulos, N.; Inoubli, M.H. Monitoring Olive Oil Mill Wastewater Disposal Sites Using Sentinel-2 and PlanetScope Satellite Images: Case Studies in Tunisia and Greece. *Agronomy* **2021**, *12*, 90. [CrossRef]
21. Sierra, O. Diagraphies différeées. Bases de L'interprétation. In *Tome 2, Interprétation des Données Diagraphiques. Bulletin des Centres de Recherches Exploration*; Production Elf Aquitaine: Courbevoie, France, 1985.
22. Ellis, D.V.; Singer, J.M. *Well Logging for Earth Scientists*; Springer: Berlin/Heidelberg, Germany, 2007. [CrossRef]
23. Liu, H. *Principles and Applications of Well Logging*; Springer: Berlin/Heidelberg, Germany, 2017. [CrossRef]
24. Chapellier, D. *Well Logging in Hydrogeology*; A.A. Balkema: Rotterdam, The Netherlands, 1992.
25. Bassiouni, Z. *Theory, Measurement and Interpretation of Well Logs*; SPE Text Book Series (Vol. 4); Society of Petroleum Engineers: Richardson, TX, USA, 1994; ISBN 978-1-55563-056-0.
26. Luthi, S. *Geological Well Logs: Their Use in Reservoir Modeling*; Springer: Berlin/Heidelberg, Germany, 2001; ISBN 978-3-540-67840-3.
27. Telford, W.C.; Geldard, B.P.; Sheriff, R.E. *Applied Geophysics*, 1st ed.; Cambridge University Press: London, UK, 1976.
28. Glover, W.G.P. *Petrophysics MSc Course Notes*; University of Aberdeen: Aberdeen, UK, 2012.
29. Keller, G.V.; Frischknecht, F.C. *Electrical Methods in Geophysical Prospecting*; Pergamon Press Inc.: Oxford, UK, 1966.
30. Ibraheem, I.M.; El-Qady, G. Hydrogeophysical Investigations at El-Nubariya-Wadi El-Natrun Area, West Nile Delta, Egypt. In *Groundwater in the Nile Delta*; Negm, A., Ed.; The Handbook of Environmental Chemistry; Springer: Cham, Switherland, 2019; Volume 73, pp. 235–271.
31. Ibraheem, I.M.; Othman, A.; Ghazala, H. Pliocene Aquifer Characterization Using TEM and VES Geophysical Techniques: Case Study at the Area to the East of Wadi El-Natrun City, West Nile Delta, Egypt. In *Sustainability of Groundwater in the Nile Valley, Egypt*; Negm, A.M., El-Rawy, M., Eds.; Earth and Environmental Sciences Library; Springer: Cham, Switherland, 2022; pp. 235–266. [CrossRef]
32. Archie, G.E. The electrical resistivity log as an aid in determining some reservoir characteristics. *Pet. Trans. AIME* **1942**, *146*, 54–62. [CrossRef]
33. Sauerheber, R.; Heinz, B. Temperature effects on conductivity of seawater and physiologic saline, mechanism and significance. *J. Chem. Sci.* **2015**, *6*, 4172. [CrossRef]
34. Dobrin, M.B. *Introduction to Geophysical Prospecting*; Mcgraw-Hill: New York, NY, USA, 1976.
35. Lowrie, W. *Fundamentals of Geophysics*, 2nd ed.; Cambridge University Press: Cambridge, UK, 2007.
36. Othman, A.A.; Beshr, A.M.; Abd El-Gawad, A.M.S.; Ibraheem, I.M. Hydrogeophysical investigation using remote sensing and geoelectrical data in southeast Hiw, Qena, Egypt. *Geocarto Int.* **2022**, *37*, 14241–14260. [CrossRef]
37. Kleh, M.; Eichorst, F.; Schafer, A. Facies interpretation from wells logs applied to the tertiary lower Rhine basin fill. *Neth. J. Geosci.* **2002**, *2*, 167–176.
38. Hsieh, B.Z.; Lewis, C.; Lin, Z.S. Lithology identification of aquifers from geophysical well logs and fuzzy logic analysis: Shui-Lin Area, Taiwan. *Comput. Geosci. J.* **2005**, *31*, 263–275. [CrossRef]
39. Guellala, R.; Inoubli, M.H.; Amri, F. *Apports des Diagraphies à l_Etude des Alluvions Quaternaires (Ghardimaou, Tunisie): Applications Hydrogeologiques*; Service Géologique de Tunisie: Tunis, Tunisia, 2010; pp. 57–68.
40. Ben Lasmar, R.; Guellala, R.; Sarsar Naouali, B.; Triki, L.; Inoubli, M.H. Contribution of geophysics to the management of water resources: Case of the Ariana agricultural sector (Eastern Mejerda Basin, Tunisia). *Nat. Resour. Res.* **2014**, *23*, 367–377. [CrossRef]
41. Castany, G. *Principes et Méthodes de l_Hydrogéologie*; Dunod Université, Bordas: Paris, France, 1982.
42. Harold, M.M.; Ernesto, O.; Harry, P.; Leonard, T. A resistivity computation method for layered earth models. *Geophysics* **2012**, *31*, 192–203. [CrossRef]
43. Asfahani, J. Geoelectrical investigation for characterizing the hydrogeological conditions in semi-arid region in Khanasser valley, Syria. *J. Arid. Environ.* **2007**, *68*, 31–52. [CrossRef]
44. Guellala, R.; Abidi, M.; Balti, N.; Inoubli, M.H. Prospection géophysique pour la recherche d'eau souterraine dans le Nord-Ouest de la Tunisie. *J. Des Sci. Hydrogeol.* **2016**, *61*, 636–645. [CrossRef]
45. Kouamé, K.F. Hydrogéologie des Aquifères Discontinus de la Région Semi Montagneuse de Man-Danané (Ouest de la Côte d'Ivoire). Apport des Données des Images Satellitales et des Méthodes Statistiques et Fractales à L'élaboration d'un Système D'information Hydrogéologique à Référence Spatiale. Ph.D. Thesis, Université de Cocody, Abidjan, Côte d'Ivoire, 1999.
46. Jourda, J.P.; Saley, M.B.; Djagoua, E.V.; Kouamé, K.J.; Biemi, J.; Razack, M. Utilisation des donneés ETM + de Landsat et d'un SIG pour l'évaluation du potentiel en eau souterraine dans le milieu fissure precambrien de la région de Korhogo (nord de la Côté d'Ivoire): Approche par analyse multicritère et test de validation. *Télédétection* **2006**, *5*, 339–357.
47. Koffi, A.S.; Ait Fora, A.; Elbelriti, H.; El Gasmi, H. Extraction par télédétection des réseaux de fractures majeurs à partir de l'image Landsat de la région d'Abidjan en Côte D'ivoire. *Sci. Lib Ed. Mersenne* **2013**, *5*, 1–16.
48. Ennabli, M. Etude Hydrogéologique des Aquifères du Nord-Est de la Tunisie Pour Une gestionintégrée des Ressources en Eau. Ph.D. Thesis, Nice, Paris, France, 1980.

49. Othman, A.A.; Ibraheem, I.M. Origin of El-Maghara Anticlines, North Sinai Peninsula, Egypt: Insights from Gravity Data Interpretation Using Edge Detection Filters. *Arab. J. Sci. Eng.* **2024**, *49*, 863–882. [CrossRef]
50. Dlala, M. Evolution Géodynamique et Tectonique Superposées en Tunisie: Implications sur la Tectonique Récente et la Sismicité. Ph.D. Thesis, Université de Tunis EL Manar, Tunis, Tunisia, 1995.
51. Crampon, N. L'extrême Nord Tunisien. Aperçu stratigraphique, pétrologique et structural. Livre jubilaire de M.Solignac. *Ann. Mines Geol.* **1973**, *26*, 49–85.